

Resonance nesting and mode degeneracy of bilayer spherical dielectric cavities within zero-index materials

Nuo Wang,¹ Yun Ma,¹ Qi Liu,^{1,2} Yu Tian,^{1,2} Yuye Wang ^{3,4} Qihuang Gong,^{1,2,5,6,7} and Ying Gu ^{1,2,5,6,7,*}

¹State Key Laboratory for Mesoscopic Physics, Department of Physics, Peking University, Beijing 100871, China

²Frontiers Science Center for Nano-optoelectronics & Collaborative Innovation Center of Quantum Matter & Beijing Academy of Quantum Information Sciences, Peking University, Beijing 100871, China

³School of Precision Instruments and Optoelectronics Engineering, Tianjin University, Tianjin 300072, China

⁴Key Laboratory of Optoelectronic Information Technology (Ministry of Education), Tianjin University, Tianjin 300072, China

⁵Collaborative Innovation Center of Extreme Optics, Shanxi University, Taiyuan, Shanxi 030006, China

⁶Peking University Yangtze Delta Institute of Optoelectronics, Nantong 226010, China

⁷Hefei National Laboratory, Hefei 230088, China



(Received 21 May 2023; accepted 21 August 2023; published 14 September 2023)

Zero-index materials (ZIMs) have many peculiar properties such as supercoupling, directional radiation, and large optical nonlinearity because of the near-zero electromagnetic parameters. Additionally, the index contrast between the cavity and the ZIM can approach infinity, resulting in exotic properties such as resonance nesting and mode degeneracy. However, the mode characteristics of bilayer spherical dielectric cavities within ZIMs have not been studied thoroughly. Here, we investigate the resonance nesting and mode degeneracy effect in bilayer spherical dielectric cavities embedded in ZIMs. First, we analytically deduce the Mie resonance condition for each eigenmode of the bilayer spherical dielectric cavities. Based on the resonance conditions, we find the resonance nesting effect, in which a set of cavities with different outer radii can possess the same type of resonance at the same wavelength. We also reveal the mode degeneracy effect, wherein the modes with different angular mode numbers such as 2^l -TM and 2^{l+1} -TE can be degenerated. Superior to monolayer cavities, the electric field distribution in bilayer cavities can be manipulated by changing the inner radius. The mode degeneracy in the bilayer cavity only happens with some specific radii, which is different from the case in the monolayer cavity where the mode degeneracy always exists. These results can not only improve our understanding of cavities within ZIMs, but can also have potential applications in deformable devices and quantum information processes.

DOI: [10.1103/PhysRevA.108.033508](https://doi.org/10.1103/PhysRevA.108.033508)

I. INTRODUCTION

Zero-index materials (ZIMs), whose relative permittivity or/and relative permeability are near zero, can be classified as ϵ -near-zero (ENZ), μ -near-zero (MNZ), and both ϵ - and μ -near-zero (EMNZ) materials. They have been experimentally realized in various materials including metals [1,2], doped semiconductors [3,4], phononic materials [5,6], and structured materials such as waveguides [7], photonic crystals (PCs) [8,9], and metamaterials [10,11]. ZIMs have many attractive properties in light manipulation and light-matter interaction, such as directive emission [12–14], supercoupling [15–17], large optical nonlinearity [4,18], nonreciprocal and nonlocal effects enhancement [19–21], and resonance pinning effect [22,23]. These fundamental studies on ZIMs may have some applications in phase pattern design [9,24], optical antennas [22,23], cloaking [25], optical nanocircuits [26,27], bending waveguides [28,29], etc.

Owing to the extreme parameter and the decoupling of temporal and spatial field variations, studies combining ZIMs and resonant cavities have shown many exotic properties, such

as the geometry-invariant eigenfrequencies [30] and nonradiating spatially electrostatic modes of open ENZ cavities [31]. The above studies mainly focused on the dipole resonance of a dielectric cavity within a ZIM, but the behaviors of higher-order resonances have not been studied systematically. By investigating the resonance of a spherical cavity embedded in an infinite ZIM, the resonance conditions for every eigenmode have been deduced and the resonance nesting and degeneracy effect have been found [32]. If a monolayer structure changes to be bilayer, there may be some special properties. For example, when a metal sphere is changed to a bilayer core-shell structure, the plasmon modes will hybridize and couple with each other, resulting in a tunable plasmon resonance [33,34]. However, the combination of ZIMs and bilayer cavities has not been studied yet; it can possess both the characteristic of cavities within ZIMs and bilayer structures.

In this work, we find that the resonance nesting and mode degeneracy effects exist in bilayer spherical dielectric cavities within ZIMs. First, we apply Mie theory to analytically deduce the resonance condition for every eigenmode of a bilayer spherical dielectric cavity within a ZIM. Interestingly, for the same inner radius, a series of cavities with different outer radii can possess the same type of resonance at a fixed wavelength, that is, the resonance nesting effect. We also reveal that when

*Corresponding author: ygu@pku.edu.cn

the inner radii have some special values, the 2^l -TM (TE) and 2^{l+1} -TE (TM) modes have the same resonance frequency for the ENZ (MNZ) background while the 2^l -TM and 2^l -TE modes have the same resonance frequency for the EMNZ background, i.e., the mode degeneracy effect. It should be pointed out that this degeneracy originates from the infinite index contrast between the second layer of the cavity and the ZIM. It is worth mentioning that although the resonance nesting and mode degeneracy have been found in monolayer cavities [32], the situation in the bilayer case is superior to that in the monolayer case. Specifically, the electric field distribution in the bilayer case can be modulated by varying the inner radius, while the electric field distributions in monolayer spherical cavities cannot be changed. This unique property can be used to realize deformable resonant devices with variable field distributions. The modes in the monolayer case are always degenerate, which cannot be controlled by changing the radius, while the mode degeneracy only exists when the bilayer cavity has some special radii, which can be controlled by changing the cavity's size. This innovative controllability can be used to control the degeneracy and choose which mode will be excited. Moreover, the analytical results are verified by full-wave simulation (see Appendix G). The resonance nesting and mode degeneracy effects not only have direct significance in light-matter interaction but also can be applied to deformable devices.

The paper is organized as follows. In Sec. II, we set up the physical model and deduce the resonance conditions to analyze the mode properties of this system. The resonance nesting and mode degeneracy effects for the ENZ, MNZ, and EMNZ cases are demonstrated in Sec. III. Some realistic situations and potential applications are discussed in Sec. IV. Finally, we conclude in Sec. V.

II. MIE RESONANCE CONDITIONS OF THE BILAYER SPHERICAL CAVITY WITHIN THE ZIM

The resonance conditions of all orders for monolayer spherical cavity within ENZ, MNZ, and EMNZ materials have been studied completely [32]. Based on this, the resonance nesting effect and the previously unknown resonance degeneracy in the monolayer cavity have been discovered. However, the mode characteristic of a bilayer cavity embedded in a ZIM has not been studied yet, which may possess more specific properties of resonance nesting and mode degeneracy. Such unique effects may provide additional principles to control the light propagation.

Here, for the case where a bilayer sphere cavity is embedded in a ZIM, we expand the electromagnetic field in Mie bases [35,36] and obtain the resonance conditions by utilizing the boundary conditions. The structure we investigated is a bilayer cavity embedded in the infinite ZIM, as schematically shown in Fig. 1. The bilayer cavity includes a dielectric sphere (region I, in light green) and a dielectric concentric shell (region II, in white). The sphere has a radius R_1 , dielectric constant ϵ_1 and magnetic permeability μ_1 ; the concentric shell has a thickness $R_2 - R_1$, dielectric constant ϵ_2 and magnetic permeability μ_2 ; the infinite ZIM (region III, in light blue) has a dielectric constant ϵ_3 and magnetic permeability μ_3 . We assume the ZIM is infinite for the pur-

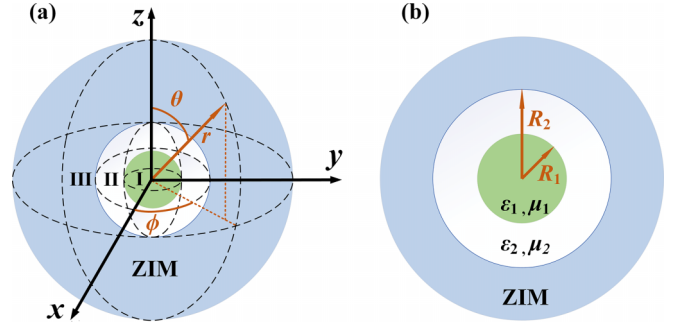


FIG. 1. The schematic diagram of a bilayer dielectric spherical cavity within a ZIM. (a) is the three-dimensional diagram and (b) is the yz section.

pose of obtaining simple analytical formulas. But the results where the ZIM is finite will be consistent with our analytical results when the ZIM is several wavelengths thick (see the Discussion section for details). For convenience, the wave numbers in regions I, II, and III are denoted by k_1 , k_2 , and k_3 respectively, and R_1 and R_2 are called the inner radius and outer radius, respectively. The eigenmodes of spherical cavities are classified as TM modes and TE modes with the vanishment of the radial component of the magnetic and electric field, respectively. The TM (TE) mode with mode number i , l , m is called the TM_{ilm} (TE_{ilm}) mode where i can be o or e which means odd mode or even mode, respectively; l is the angular mode number or the multipole order, such as $l = 1$ for dipole mode and $l = 2$ for quadrupole mode; m is the azimuthal mode number satisfying $|m| \leq |l|$. We can let $m = 0$, $i = e$ to get the resonance conditions because m and i only decide on angular distribution while the boundary condition is only associated with the radial distribution. Therefore, the resonance can be categorized as 2^l -TM and 2^l -TE.

We first consider the 2^l -TM modes. According to Mie theory, the electromagnetic field of a spherically symmetric system can be expressed as the linear combination of two sets of vector spherical harmonics \mathbf{M} and \mathbf{N} (see Appendix A). Because the magnetic field has no radial component, the magnetic field of the TM mode only includes the \mathbf{M} . By normalizing the coefficient of $\mathbf{M}_l^{(2)}$ in region I, the electromagnetic field can be written as

$$\mathbf{H}_{\text{TM}}^l = \begin{cases} \mathbf{M}_l^{(2)} + A_1 \mathbf{M}_l^{(1)}, & r < R_1 \\ B_1 \mathbf{M}_l^{(2)} + C_1 \mathbf{M}_l^{(1)}, & R_1 < r < R_2, \\ D_1 \mathbf{M}_l^{(3)}, & r > R_2 \end{cases} \quad (1)$$

$$\mathbf{E}_{\text{TM}}^l = \begin{cases} -\frac{k_1}{i\epsilon_1 \epsilon_0 \omega} (\mathbf{N}_l^{(2)} + A_1 \mathbf{N}_l^{(1)}), & r < R_1 \\ -\frac{k_2}{i\epsilon_2 \epsilon_0 \omega} (B_1 \mathbf{N}_l^{(2)} + C_1 \mathbf{N}_l^{(1)}), & R_1 < r < R_2, \\ -\frac{k_3}{i\epsilon_3 \epsilon_0 \omega} D_1 \mathbf{N}_l^{(3)}, & r > R_2 \end{cases}$$

where A_1 , B_1 , C_1 , and D_1 are the coefficients to be solved, $\mathbf{M}_l^{(j)} = -\frac{\partial P_l}{\partial \theta} z_l^{(j)}(kr) \hat{e}_\phi$, and $\mathbf{N}_l^{(j)} = \frac{z_l^{(j)}(kr)}{kr} l(l+1) P_l \hat{e}_r + \frac{1}{kr} \frac{\partial [(kr) z_l^{(j)}(kr)]}{\partial (kr)} \frac{\partial P_l}{\partial \theta} \hat{e}_\theta$. $z_l^{(1)}$ is the spherical Bessel functions labeled as j_l ; $z_l^{(2)}$ is the spherical Neumann functions labeled as n_l ; $z_l^{(3)}$ and $z_l^{(4)}$ are the first and second kind

of spherical Hankel functions labeled as $h_l^{(1)}$ and $h_l^{(2)}$, respectively, where $h_l^{(1)} = j_l + in_l$ and $h_l^{(2)} = j_l - in_l$. P_l is the Legendre functions with $P_l(\cos \theta) = \frac{1}{2^l l!} \frac{d^l}{d \cos^l \theta} (\cos^2 \theta - 1)^l$.

According to the boundary conditions at $r = R_1$ and $r = R_2$, we can get the general resonance conditions for 2^l -TM modes of bilayer spherical cavity embedded in an arbitrary medium (see Appendix B for details):

$$\frac{\begin{vmatrix} \frac{\varepsilon_3}{\varepsilon_2} \zeta'_l(\rho_{22}) & \xi'_l(\rho_{32}) \\ \zeta_l(\rho_{22}) & \frac{k_2}{k_3} \xi_l(\rho_{32}) \end{vmatrix}}{\begin{vmatrix} \frac{\varepsilon_3}{\varepsilon_2} \eta'_l(\rho_{22}) & \xi'_l(\rho_{32}) \\ \eta_l(\rho_{22}) & \frac{k_2}{k_3} \xi_l(\rho_{32}) \end{vmatrix}} = \frac{\begin{vmatrix} \frac{\varepsilon_1}{\varepsilon_2} \zeta'_l(\rho_{21}) & \eta'_l(\rho_{11}) \\ \zeta_l(\rho_{21}) & \frac{k_2}{k_1} \eta_l(\rho_{11}) \end{vmatrix}}{\begin{vmatrix} \frac{\varepsilon_1}{\varepsilon_2} \eta'_l(\rho_{21}) & \eta'_l(\rho_{11}) \\ \eta_l(\rho_{21}) & \frac{k_2}{k_1} \eta_l(\rho_{11}) \end{vmatrix}}, \quad (2)$$

in which we let $x \equiv kr$, $\eta_l(x) \equiv x j_l(x)$, $\zeta_l(x) \equiv x n_l(x)$, $\xi_l(x) \equiv x h_l^{(1)}(x)$; $\rho_{11} \equiv k_1 R_1$, $\rho_{21} \equiv k_2 R_1$, $\rho_{22} \equiv k_2 R_2$, $\rho_{32} \equiv k_3 R_2$.

When the background is a ZIM, $k_3 \approx 0$, so $\xi_l(k_3 r)$ can be expanded as a power series of $(k_3 r)^{-1}$:

$$\xi_l(k_3 r) \approx ik_3 r [n_l(k_3 r)] = i \sum_{n=0}^{\infty} a_n (k_3 r)^{2n-1} \approx ia_0 (k_3 r)^{-1},$$

$$\xi'_l(k_3 r) \approx i(-l)[a_0 (k_3 r)^{-l-1}], \quad (3)$$

in which, a_0 is a real constant number. Therefore, the resonance condition for the TM mode of a bilayer spherical cavity within an infinite ZIM background can be obtained as

$$\frac{l \zeta_l(\rho_{22}) + \frac{\varepsilon_3}{\varepsilon_2} \rho_{22} \zeta'_l(\rho_{22})}{l \eta_l(\rho_{22}) + \frac{\varepsilon_3}{\varepsilon_2} \rho_{22} \eta'_l(\rho_{22})} = \frac{\begin{vmatrix} \frac{\varepsilon_1}{\varepsilon_2} \zeta'_l(\rho_{21}) & \eta'_l(\rho_{11}) \\ \zeta_l(\rho_{21}) & \frac{k_2}{k_1} \eta_l(\rho_{11}) \end{vmatrix}}{\begin{vmatrix} \frac{\varepsilon_1}{\varepsilon_2} \eta'_l(\rho_{21}) & \eta'_l(\rho_{11}) \\ \eta_l(\rho_{21}) & \frac{k_2}{k_1} \eta_l(\rho_{11}) \end{vmatrix}}. \quad (4)$$

Because of the extreme parameters of ZIMs, the terms $\xi_l(\rho_{32})$ and $\xi'_l(\rho_{32})$ are in opposite phases so this equation does not have any imaginary component (see Appendix C for a discussion of phase). Therefore, the resonance condition for the ZIM case can be exactly solved in the real number field and the cavity can possess an ideal resonance while the general resonance condition can only be exactly solved in the complex number field. Moreover, because the refractive index of the ZIM is zero, this resonance does not depend on μ_3 . Therefore, the TM modes for the ENZ ($\varepsilon_3 = 0$) case and the EMNZ ($\varepsilon_3 = 0, \mu_3 = 0$) case always have the same resonance conditions, shown in the following equation (5).

Because $\varepsilon_3 \approx 0$ for the ENZ and EMNZ cases, the condition can be simplified as

$$\frac{\zeta_l(\rho_{22})}{\eta_l(\rho_{22})} = \frac{\begin{vmatrix} \frac{\varepsilon_1}{\varepsilon_2} \zeta'_l(\rho_{21}) & \eta'_l(\rho_{11}) \\ \zeta_l(\rho_{21}) & \frac{k_2}{k_1} \eta_l(\rho_{11}) \end{vmatrix}}{\begin{vmatrix} \frac{\varepsilon_1}{\varepsilon_2} \eta'_l(\rho_{21}) & \eta'_l(\rho_{11}) \\ \eta_l(\rho_{21}) & \frac{k_2}{k_1} \eta_l(\rho_{11}) \end{vmatrix}}. \quad (5)$$

In the following, with the same procedure, we can analytically obtain the resonance conditions for the 2^l -TE mode. Its electromagnetic fields inside and outside the cavity can be

expressed as

$$\mathbf{E}_{\text{TM}}^l = \begin{cases} \mathbf{M}_l^{(2)} + A_2 \mathbf{M}_l^{(1)}, & r < R_1 \\ B_2 \mathbf{M}_l^{(2)} + C_2 \mathbf{M}_l^{(1)}, & R_1 < r < R_2, \\ D_2 \mathbf{M}_l^{(3)}, & r > R_2 \end{cases} \quad (6)$$

$$\mathbf{H}_{\text{TM}}^l = \begin{cases} \frac{k_1}{i\mu_1 \mu_0 \omega} (\mathbf{N}_l^{(2)} + A_2 \mathbf{N}_l^{(1)}), & r < R_1 \\ \frac{k_2}{i\mu_2 \mu_0 \omega} (B_2 \mathbf{N}_l^{(2)} + C_2 \mathbf{N}_l^{(1)}), & R_1 < r < R_2, \\ \frac{k_3}{i\mu_3 \mu_0 \omega} D_2 \mathbf{N}_l^{(3)}, & r > R_2 \end{cases}$$

where A_2, B_2, C_2 , and D_2 are the coefficients to be solved.

Based on the boundary conditions, the resonance condition for the TE modes of a bilayer spherical cavity within an infinite ZIM background can be obtained by using the same method as that for the TM case (see Appendix B for details):

$$\frac{l \zeta_l(\rho_{22}) + \frac{\mu_3}{\mu_2} \rho_{22} \zeta'_l(\rho_{22})}{l \eta_l(\rho_{22}) + \frac{\mu_3}{\mu_2} \rho_{22} \eta'_l(\rho_{22})} = \frac{\begin{vmatrix} \frac{\mu_1}{\mu_2} \zeta'_l(\rho_{21}) & \eta'_l(\rho_{11}) \\ \zeta_l(\rho_{21}) & \frac{k_2}{k_1} \eta_l(\rho_{11}) \end{vmatrix}}{\begin{vmatrix} \frac{\mu_1}{\mu_2} \eta'_l(\rho_{21}) & \eta'_l(\rho_{11}) \\ \eta_l(\rho_{21}) & \frac{k_2}{k_1} \eta_l(\rho_{11}) \end{vmatrix}}. \quad (7)$$

Furthermore, for MNZ and EMNZ materials, $\mu_3 \approx 0$, the condition can be simplified as

$$\frac{\zeta_l(\rho_{22})}{\eta_l(\rho_{22})} = \frac{\begin{vmatrix} \frac{\mu_1}{\mu_2} \zeta'_l(\rho_{21}) & \eta'_l(\rho_{11}) \\ \zeta_l(\rho_{21}) & \frac{k_2}{k_1} \eta_l(\rho_{11}) \end{vmatrix}}{\begin{vmatrix} \frac{\mu_1}{\mu_2} \eta'_l(\rho_{21}) & \eta'_l(\rho_{11}) \\ \eta_l(\rho_{21}) & \frac{k_2}{k_1} \eta_l(\rho_{11}) \end{vmatrix}}. \quad (8)$$

It should be emphasized that the resonance condition of the bilayer spherical cavity within a ZIM is general. For example, it is true for arbitrary wavelengths such that the background material is a ZIM. Also, it remains valid for any value of the electromagnetic parameters of the bilayer cavity. Furthermore, the deduction of resonance conditions can be easily extended to a multilayer spherical cavity within the ZIM.

The resonance condition [32] of the monolayer case has only one geometry variable resulting in it being a set of points in the R axis (R is the radius of the monolayer cavity), but the resonance condition of the bilayer cavity has two geometry variables: the inner radius R_1 and the outer radius R_2 , resulting in it being a set of curves in the R_1, R_2 coordinates. Both the points for the monolayer case and the curves for the bilayer case imply the existence of resonance nesting and mode degeneracy. Additionally, by some mathematical transformation, we verified that the resonance condition of the bilayer cavity is the same as that of the monolayer cavity when $R_1 = 0$ or $R_1 = R_2$.

III. RESULTS

A. Resonance nesting of bilayer cavities within ZIMs

There is a resonance nesting effect in monolayer cavities within the ENZ background [32]. With the same background, we predict that this effect should exist in bilayer cavities. Take the 2-TM mode as an example (similar discussions on other modes can be found in Appendix D1); according to Eq. (5), the curves satisfying the resonance condition for the case where $\lambda = 630$ nm, $\varepsilon_1 = 2.25$, $\mu_1 = 1$, $\varepsilon_2 = 1$, $\mu_2 = 1$,

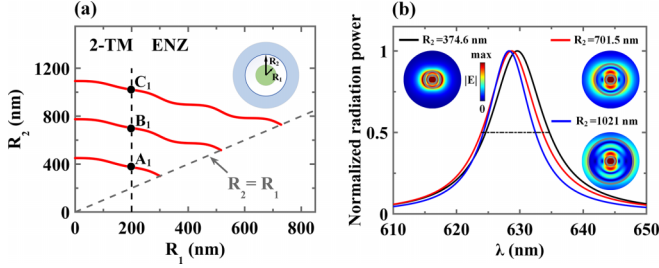


FIG. 2. The resonance nesting of the 2-TM mode for the ENZ case. (a) The curves satisfying the resonance condition. These curves have many branches, representing the multiplicity of solutions of the resonance condition. Here, $\lambda = 630$ nm, $\epsilon_1 = 2.25$, $\mu_1 = 1$, $\epsilon_2 = 1$, $\mu_2 = 1$, $\epsilon_3 = 0$, $\mu_3 = 1$. (b) The normalized power spectra and electric fields (modulus) taken at A_1 , B_1 , and C_1 in (a). The peaks of resonance and the consistency of the electric field evidence the existence of resonance nesting.

$\epsilon_3 = 0$, and $\mu_3 = 1$ are plotted in Fig. 2(a). It is found that the resonance curves have many branches, i.e., when $R_1 = 200$ nm, a set of R_2 represented by the nested points A_1 , B_1 , and C_1 can satisfy the resonance condition. As shown in Fig. 2(b), the peaks of the power spectra at these three points are almost at 630 nm; that is, for the same inner radius, a series of cavities with different outer radii can possess the same type of resonance at a fixed wavelength, called the resonance nesting effect. It can be seen from the insets of Fig. 2(b) that the electric field distributions inside three cavities are completely consistent while just the number of wave nodes increases with R_2 . These evidence the existence of resonance nesting. Moreover, there are a few blueshifts of resonant wavelengths in radiation power spectra in Fig. 2(b) due to the imaginary part of $\epsilon_3 = 0.01i$. The resonant wavelengths of three nesting cavities deviate slightly from the ideal value. The electric field distribution of the 2-TM mode is discontinuous at the interface because the radical component of the electric field suddenly changes. Especially at the interface between the cavity and the ENZ, the electric field is drastically enhanced due to the ultrahigh contrast ratio of ϵ_2 and ϵ_3 .

As we expected, although the resonance conditions for the ENZ, MNZ, and EMNZ cases are different, the resonance nesting effect also appears in the bilayer spherical cavities embedded in the MNZ and EMNZ backgrounds (see Appendixes D2 and D3 for details). Therefore, the resonance nesting is a universal property of bilayer spherical cavities within ZIMs.

B. Difference in resonance nesting between bilayer cavities and monolayer cavities within ZIMs

The difference in the resonance nesting effect of bilayer cavities compared to that of monolayer cavities is that the electric field distributions in the bilayer spherical cavities can be manipulated by changing the inner radius while maintaining resonance nesting. This result is very different from that in the monolayer cavities [32] where the electric field distribution is unchangeable. For the electromagnetic field expressions, Eqs. (1) and (6), the coefficients of field will approach infinity when resonance occurs so that it is difficult

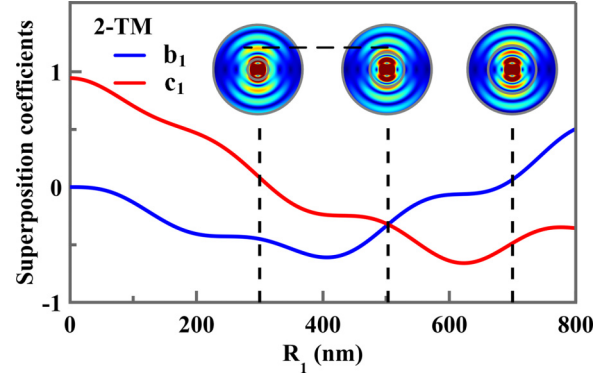


FIG. 3. The superposition coefficients of the field in region II for the 2-TM mode. The variation of superposition coefficients results in the modulation of electric field distribution. The insets are corresponding electric fields at different R_1 .

to analyze the field distribution. Therefore, we can rebuild the expression by normalizing A_1 for TM modes in Eq. (1) and normalizing A_2 for TE modes in Eq. (6). Let us take the TM modes as an example:

$$\mathbf{H}_{\text{TM}}^{ilm} = \begin{cases} \mathbf{M}_{ilm}^{(1)}, & r < R_1 \\ b_1 \mathbf{M}_{ilm}^{(2)} + c_1 \mathbf{M}_{ilm}^{(1)}, & R_1 < r < R_2, \\ d_1 \mathbf{M}_{ilm}^{(3)}, & r > R_2 \end{cases} \quad (9)$$

$$\mathbf{E}_{\text{TM}}^{ilm} = \begin{cases} -\frac{k_1}{i\epsilon_1 \epsilon_0 \omega} \mathbf{N}_{ilm}^{(1)}, & r < R_1 \\ -\frac{k_2}{i\epsilon_2 \epsilon_0 \omega} (b_1 \mathbf{N}_{ilm}^{(2)} + c_1 \mathbf{N}_{ilm}^{(1)}), & R_1 < r < R_2, \\ -\frac{k_3}{i\epsilon_3 \epsilon_0 \omega} d_1 \mathbf{N}_{ilm}^{(3)}, & r > R_2 \end{cases}$$

where b_1 , c_1 are the new coefficients. By substituting the general resonance condition, Eq. (2), into them, we can obtain

$$b_1 = \frac{B_1}{A_1} = \frac{\left| \begin{array}{cc} \eta'_l(\rho_{11}) & \frac{\epsilon_1}{\epsilon_2} \eta'_l(\rho_{21}) \\ \frac{k_2}{k_1} \eta_l(\rho_{11}) & \eta_l(\rho_{21}) \end{array} \right|}{\left| \begin{array}{cc} \frac{\epsilon_1}{\epsilon_2} \zeta'_l(\rho_{21}) & \frac{\epsilon_1}{\epsilon_2} \eta'_l(\rho_{21}) \\ \zeta_l(\rho_{21}) & \eta_l(\rho_{21}) \end{array} \right|};$$

$$c_1 = \frac{C_1}{A_1} = \frac{\left| \begin{array}{cc} \eta'_l(\rho_{11}) & \frac{\epsilon_1}{\epsilon_2} \zeta'_l(\rho_{21}) \\ \frac{k_2}{k_1} \eta_l(\rho_{11}) & \zeta_l(\rho_{21}) \end{array} \right|}{\left| \begin{array}{cc} -\frac{\epsilon_1}{\epsilon_2} \zeta'_l(\rho_{21}) & -\frac{\epsilon_1}{\epsilon_2} \eta'_l(\rho_{21}) \\ \zeta_l(\rho_{21}) & \eta_l(\rho_{21}) \end{array} \right|}. \quad (10)$$

The coefficients b_1 and c_1 are only dependent on R_1 and the electromagnetic parameters of the bilayer cavity. Therefore, for a fixed R_1 , the field distributions inside the cavity within different backgrounds are identical while just R_2 and the number of wave nodes are different.

For a monolayer dielectric cavity embedded in a ZIM, once the mode numbers are selected, its field distribution is fixed [32], but this is not the case in a bilayer cavity because the field in the region II is decided by the superposition coefficients. For the 2-TM mode, the coefficients b_1 , c_1 as a function of R_1 are shown in Fig. 3. It is found that the position of the maximum of the electric field in the region II changes with R_1 (the insets of Fig. 3). Similar analysis is true for the TE mode (see Appendix F).

The cavities within ENZ materials can support spatially “electrostatic” eigenmodes whose resonant frequency is independent of the geometry of the ENZ materials bounded by perfectly electric conducting (PEC) walls. This result can be used to realize deformable resonant devices [30]. Owing to the tunability of bilayer cavities, deformable devices with variable electric fields can be achieved.

Therefore, the resonance nesting effect exists in bilayer cavities within ZIMs including the ENZ, MNZ, and EMNZ cases; i.e., for the same inner radius, a series of cavities with different outer radii can possess the same type of resonance at a fixed wavelength. The mode characteristics for different backgrounds is quite different; for example, the 2-TM mode in the ENZ case is a nonradiating mode but not in the MNZ cases [31]. The main text only includes the results of the 2-TM mode, while the same findings hold true for other modes as well, such as the 2-TE, 4-TM, and 4-TE modes (see Appendixes D1–D3). It is worth mentioning that the resonance nesting effect of bilayer cavities is superior to that in the monolayer case because the electromagnetic field distribution of the bilayer cavity can be tuned by changing the inner radius.

C. Mode degeneracy of bilayer cavities within ZIMs

There is mode degeneracy between the 2^l -TM and 2^{l+1} -TE modes in monolayer spherical cavities within the ENZ background [32]. With the same background, it seems that this effect should also exist in bilayer cavities. But the situation is very different. From the following analysis, it is found that the 2^l -TM and 2^{l+1} -TE modes of bilayer cavities within the ENZ background are degenerated only at some special nested points. In what follows, we first analytically prove this conclusion based on the resonance conditions. According to Eq. (7), the 2^{l+1} -TE modes satisfy the following:

$$\frac{(l+1)\zeta_{l+1}(\rho_{22}) + \rho_{22}\zeta'_{l+1}(\rho_{22})}{(l+1)\eta_{l+1}(\rho_{22}) + \rho_{22}\eta'_{l+1}(\rho_{22})} = \frac{\left| \begin{array}{cc} \frac{\mu_1}{\mu_2}\zeta'_{l+1}(\rho_{21}) & \eta'_{l+1}(\rho_{11}) \\ \zeta_{l+1}(\rho_{21}) & \frac{k_2}{k_1}\eta_{l+1}(\rho_{11}) \end{array} \right|}{\left| \begin{array}{cc} \frac{\mu_1}{\mu_2}\eta'_{l+1}(\rho_{21}) & \eta'_{l+1}(\rho_{11}) \\ \eta_{l+1}(\rho_{21}) & \frac{k_2}{k_1}\eta_{l+1}(\rho_{11}) \end{array} \right|}. \quad (11)$$

Given the mathematical identities,

$$\begin{aligned} (l+1)\zeta_{l+1}(x) + x\zeta'_{l+1}(x) &= x\zeta_l(x), \\ (l+1)\eta_{l+1}(x) + x\eta'_{l+1}(x) &= x\eta_l(x), \end{aligned} \quad (12)$$

Eq. (11) can be simplified to

$$\frac{\zeta_l(\rho_{22})}{\eta_l(\rho_{22})} = \frac{\left| \begin{array}{cc} \frac{\mu_1}{\mu_2}\zeta'_{l+1}(\rho_{21}) & \eta'_{l+1}(\rho_{11}) \\ \zeta_{l+1}(\rho_{21}) & \frac{k_2}{k_1}\eta_{l+1}(\rho_{11}) \end{array} \right|}{\left| \begin{array}{cc} \frac{\mu_1}{\mu_2}\eta'_{l+1}(\rho_{21}) & \eta'_{l+1}(\rho_{11}) \\ \eta_{l+1}(\rho_{21}) & \frac{k_2}{k_1}\eta_{l+1}(\rho_{11}) \end{array} \right|}. \quad (13)$$

By comparing Eq. (13) with Eq. (5), it is found that the left-hand sides (LHSs) of the resonance conditions of the 2^l -TM and 2^{l+1} -TE modes are the same but the right-hand sides (RHSs) are usually unequal. However, for some special R_1 , they can be the same, allowing these two modes to be degenerate. Additionally, when R_1 is fixed at such a value,

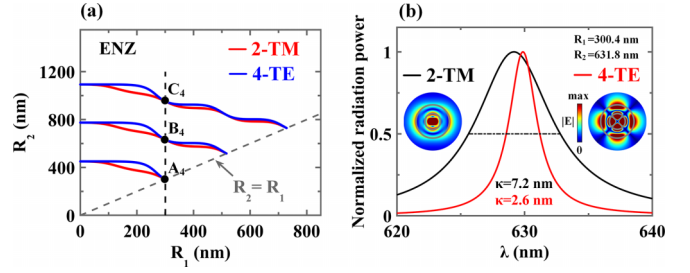


FIG. 4. The degeneracy between the 2-TM and 4-TE modes of bilayer spherical cavities for the ENZ case. (a) The resonance conditions of the 2-TM and 4-TE modes. The nested points where the red curves intersect with the blue curves represent the degeneracy. (b) The normalized radiation power spectra of the 2-TM and 4-TE modes at point B_4 . The insets are corresponding electric field distributions (modulus).

a succession of R_2 can satisfy the two resonance conditions simultaneously due to the resonance nesting and the identity between the LHSs. In other words, if one resonant cavity satisfies the degeneracy criterion, then so will all of the others that are nested with it.

Then, take the 2-TM and 4-TE modes as an example. The resonance condition curves are plotted in Fig. 4(a). The degeneracy exists at the nested points where the red curve intersects with the blue one, such as A_4 , B_4 , and C_4 with $R_1 = 300.4$ nm. The 2-TM and 4-TE modes’ radiation power spectra at point B_4 are shown in Fig. 4(b). The peaks of the power spectra are almost at 630 nm, representing the mode degeneracy. Additionally, the 4-TE mode’s linewidth and slight blueshift from the ideal resonant wavelength (630 nm) are smaller than the counterpart of the 2-TM mode because the higher-order mode suffers from less radiation loss. The resonant wavelengths of the 2-TM and 4-TE modes deviate slightly from the ideal value. The cavities at the nested points A_4 and C_4 (see Appendix E1) also exhibit the same results, demonstrating the nesting nature of degenerate points. Therefore, for the ENZ case, the 2^l -TM and 2^{l+1} -TE modes of bilayer cavities at some special nested points will be degenerated.

Similarly, the 2^{l+1} -TM and 2^l -TE modes of bilayer cavities on some special sizes will be degenerated for the MNZ case (see Appendix E2 for details) and the 2^l -TM and 2^l -TE modes of bilayer cavities on some specific sizes will be degenerated for the EMNZ case (see Appendix E3 for details). Therefore, although the degenerated modes are different, the mode degeneracy is a general property of bilayer spherical cavities within ZIMs.

D. Difference in mode degeneracy between bilayer cavities and monolayer cavities within ZIMs

The difference in the mode degeneracy effect of bilayer cavities from that of monolayer cavities is the controllability. For monolayer cavities embedded in ENZ materials, the 2^l -TM and 2^{l+1} -TE modes are always degenerated when the permeabilities of the cavity and the background media are equivalent, but for bilayer cavities, the modes only degenerate when the cavity has some specific sizes. It is challenging to separately excite the 2^l -TM or 2^{l+1} -TE mode in monolayer

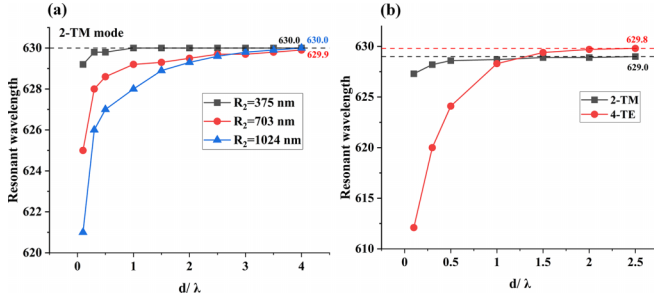


FIG. 5. (a) The resonant wavelengths of three nested cavities when the ENZ background is finite. The parameters are $R_1 = 200$ nm, $\varepsilon_1 = 2.25$, $\varepsilon_2 = 1$, $\varepsilon_3 = 0.01i$, $\mu_1 = \mu_2 = \mu_3 = 1$. The thickness of the ENZ material is labeled as d . (b) The resonant wavelengths of the 2-TM and 4-TE modes when the ENZ background is finite. The parameters are $R_1 = 300.4$ nm, $R_2 = 631.8$ nm, $\varepsilon_1 = 2.25$, $\varepsilon_2 = 1$, $\varepsilon_3 = 0.01i$, $\mu_1 = \mu_2 = \mu_3 = 1$.

cavities, but now this controllability of bilayer cavities allows us to choose which mode will be excited by altering the geometrical size. These modes will couple together and possess the coherent superposition field, so the controllability of bilayer case enables us to modulate the electromagnetic field.

The situations connected to degeneracy are thoroughly examined and listed as follows: the mode degeneracy is present in bilayer spherical dielectric cavities at some special nested points, including the degeneracy between the 2^l -TM and 2^{l+1} -TE modes for the ENZ case, 2^l -TE and 2^{l+1} -TM modes for the MNZ case, and 2^l -TM modes and 2^l -TE modes for the EMNZ case. Superior to the case of monolayer cavities, mode degeneracy of bilayer cavities and the related electromagnetic field can be controlled by changing their sizes.

IV. DISCUSSION

The situation we considered is that a bilayer spherical cavity is located in an infinite ZIM, which is unrealizable. However, according to our COMSOL simulation, within several wavelengths, the computation results will be consistent with the theoretical results. Take the ENZ case as an example; we calculated the relationship between the resonant wavelength and the thickness of the ENZ material. First, as shown in Fig. 5(a), when the thickness is 4λ , the resonant wavelengths of the 2-TM mode of three nested cavities all approach the analytical results. Also, as shown in Fig. 5(b), when the thickness is 2.5λ , the resonant wavelengths of the 2-TM and 4-TE modes both near the analytical results. Therefore, the minimum thickness needed to realize resonance nesting and mode degeneracy in this situation is about 4λ . The results in other situations are similar.

We also discuss the sensitivity of resonances to the imaginary part of the electromagnetic parameters of the zero-index materials. Take the 2-TM mode of the ENZ case as an example; the quantitative results of how the resonant wavelength and linewidth vary with the imaginary parts of ε_3 and μ_3 are shown in Fig. 6. The resonant wavelength varies by 6.4 nm while the linewidth changes from 1 nm to 41.6 nm, as the imaginary part of ε_3 increased from 0.001 to 0.05. Thus, the resonant wavelength of the TM mode is less sensitive to the imaginary part of ε_3 , but the linewidth is more sensitive.

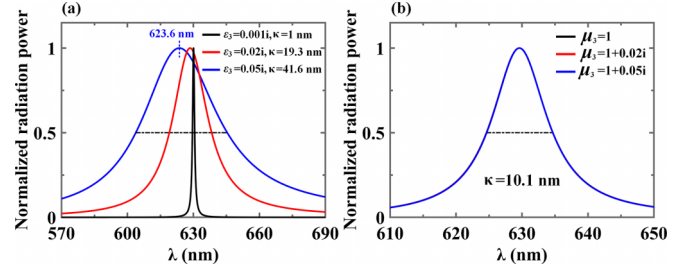


FIG. 6. (a) The resonant wavelengths and the linewidths of the 2-TM mode when the imaginary part of ε_3 of the ENZ material is considered. The parameters are $R_1 = 200$ nm, $R_2 = 374.6$ nm, $\varepsilon_1 = 2.25$, $\varepsilon_2 = 1$, $\mu_1 = \mu_2 = \mu_3 = 1$. (b) The resonant wavelengths and linewidths of the 2-TM mode when the imaginary part of μ_3 of the ENZ material is considered. The parameters are $R_1 = 200$ nm, $R_2 = 374.6$ nm, $\varepsilon_1 = 2.25$, $\varepsilon_2 = 1$, $\varepsilon_3 = 0.01i$, $\mu_1 = \mu_2 = 1$.

Moreover, as shown in Fig. 6(b), three radiation power spectra of the 2-TM mode are almost completely coincident so that the resonant wavelength and linewidth almost do not change with the imaginary part of μ_3 .

The special mode feature of cavities within ZIMs may have potential applications in cavity quantum electrodynamics (CQED) and controlling entanglement. Research on spontaneous emission of the emitter in a monolayer spherical cavity within the ZIM has been reported [37], where the inhibition and enhancement of spontaneous emission have been realized. The entanglement between emitters in ENZ waveguides has been reported [38], where the efficient long-range entanglement has been obtained, so the entanglement between emitters located in a cavity within the ZIM should also exist. These applications can be better manipulated through the flexible controllability of the bilayer cavities within ZIMs.

V. CONCLUSION

In this work, we have deduced the Mie resonance conditions for all modes of a bilayer spherical cavity embedded in ENZ, MNZ and EMNZ materials respectively. Based on the resonance conditions, the resonance nesting and mode degeneracy effects are found in this cavity system. Additionally, the electric field distribution in the bilayer cavity can be manipulated by altering the inner radius while maintaining the resonance nesting. This property is not present in the monolayer case and allows for designing deformable devices with adjustable field distribution. Also, we have found that the mode degeneracy occurs in bilayer spherical cavities with some specific radii, so that the degeneracy can be controlled by varying the cavity's size. It is superior to the monolayer situation where two modes are always degenerated, and can be used to modulate the electromagnetic field. Thus, the most unique property of the bilayer cavity compared with the monolayer cavity is the controllability of modes and electric field distributions. Moreover, the resonance nesting effect is a general consequence of cavities within ZIMs, so a similar effect should also exist in the bilayer cylindrical cavities and bilayer rectangular cavities within ZIMs. But the mode degeneracy effect discussed here results from the combination of the extreme parameters of ZIMs and spherical symmetry. These results enable flexible control of the electric field, which may

have potential applications in CQED and the manipulation of entanglement.

ACKNOWLEDGMENTS

This work was supported by the National Natural Science Foundation of China (Grant No. 11974032) and Key R&D Program of Guangdong Province (Grant No. 2018B030329001).

APPENDIX A: EXPRESSIONS OF MIE BASES \mathbf{M} AND \mathbf{N}

According to Mie theory [35,36], the Mie bases \mathbf{M} and \mathbf{N} satisfy that

$$\mathbf{M} = \nabla \times (\mathbf{r}\psi), \quad \mathbf{N} = \frac{1}{k} \nabla \times \mathbf{M}.$$

ψ is the solution of scalar wave equation $\nabla^2\psi + k^2\psi = 0$. Therefore, the Mie bases can be expressed as

$$\begin{aligned} \mathbf{M}_{elm}^{(j)} &= -\sin(m\phi) \frac{m}{\sin\theta} P_{lm}(\cos\theta) z_l^{(j)}(kr) \hat{\mathbf{e}}_\theta - \cos(m\phi) \frac{\partial P_{lm}(\cos\theta)}{\partial\theta} z_l^{(j)}(kr) \hat{\mathbf{e}}_\phi \\ \mathbf{M}_{olm}^{(j)} &= \cos(m\phi) \frac{m}{\sin\theta} P_{lm}(\cos\theta) z_l^{(j)}(kr) \hat{\mathbf{e}}_\theta - \sin(m\phi) \frac{\partial P_{lm}(\cos\theta)}{\partial\theta} z_l^{(j)}(kr) \hat{\mathbf{e}}_\phi \\ \mathbf{N}_{elm}^{(j)} &= \frac{z_l^{(j)}(kr)}{kr} l(l+1) \cos(m\phi) P_{lm}(\cos\theta) \hat{\mathbf{e}}_r + \frac{1}{kr} \frac{\partial[(kr)z_l^{(j)}(kr)]}{\partial(kr)} \cos(m\phi) \frac{\partial P_{lm}(\cos\theta)}{\partial\theta} \hat{\mathbf{e}}_\theta \\ &\quad + \frac{1}{kr} \frac{\partial[(kr)z_l^{(j)}(kr)]}{\partial(kr)} (-\sin m\phi) \frac{m}{\sin\theta} P_{lm}(\cos\theta) \hat{\mathbf{e}}_\phi \\ \mathbf{N}_{olm}^{(j)} &= \frac{z_l^{(j)}(kr)}{kr} l(l+1) \sin(m\phi) P_{lm}(\cos\theta) \hat{\mathbf{e}}_r + \frac{1}{kr} \frac{\partial[(kr)z_l^{(j)}(kr)]}{\partial(kr)} \sin(m\phi) \frac{\partial P_{lm}(\cos\theta)}{\partial\theta} \hat{\mathbf{e}}_\theta \\ &\quad + \frac{1}{kr} \frac{\partial[(kr)z_l^{(j)}(kr)]}{\partial(kr)} \cos(m\phi) \frac{m}{\sin\theta} P_{lm}(\cos\theta) \hat{\mathbf{e}}_\phi, \end{aligned} \quad (\text{A1})$$

in which P_{lm} is the associated Legendre functions with $P_{lm}(\cos\theta) = \frac{(1-\cos^2\theta)^{m/2}}{2^m l!} \frac{d^{l+m}}{d\cos^{l+m}\theta} (\cos^2\theta - 1)^l$.

APPENDIX B: GENERAL RESONANCE CONDITIONS OF BILAYER SPHERE CAVITIES WITHIN AN ARBITRARY MEDIUM

For the 2^l -TM modes, according to the boundary condition, the tangential electric field is continuous at $r = R_1$, which requires

$$\begin{aligned} \frac{k_1}{\varepsilon_1} \frac{1}{k_1 R_1} \left\{ \frac{\partial[(k_1 R_1) n_l(k_1 R_1)]}{\partial(kr)} + A_1 \frac{\partial[(k_1 R_1) j_l(k_1 R_1)]}{\partial(kr)} \right\} \\ = \frac{k_2}{\varepsilon_2} \frac{1}{k_2 R_1} \left\{ B_1 \frac{\partial[(k_2 R_1) n_l(k_2 R_1)]}{\partial(kr)} + C_1 \frac{\partial[(k_2 R_1) j_l(k_2 R_1)]}{\partial(kr)} \right\}. \end{aligned} \quad (\text{B1})$$

The tangential magnetic field is also continuous at $r = R_1$ because there is no free surface current on the interface, which requires

$$B_1 n_l(k_2 R_1) + C_1 j_l(k_2 R_1) = A_1 j_l(k_1 R_1) + n_l(k_1 R_1). \quad (\text{B2})$$

The same boundary conditions also exist at $r = R_2$, so

$$\begin{aligned} \frac{k_3}{\varepsilon_3} D_1 \frac{1}{k_3 R_2} \frac{\partial[(k_3 R_2) h_l^{(1)}(k_3 R_2)]}{\partial(kr)} \\ = \frac{k_2}{\varepsilon_2} \frac{1}{k_2 R_2} \left\{ B_1 \frac{\partial[(k_2 R_2) n_l(k_2 R_2)]}{\partial(kr)} + C_1 \frac{\partial[(k_2 R_2) j_l(k_2 R_2)]}{\partial(kr)} \right\}, \end{aligned} \quad (\text{B3})$$

$$B_1 n_l(k_2 R_2) + C_1 j_l(k_2 R_2) = D_1 h_l^{(1)}(k_3 R_2). \quad (\text{B4})$$

Let $x \equiv kr$, $\eta_l(x) \equiv x j_l(x)$, $\zeta_l(x) \equiv x n_l(x)$, $\xi_l(x) \equiv x h_l^{(1)}(x)$; $\rho_{11} \equiv k_1 R_1$, $\rho_{21} \equiv k_2 R_1$, $\rho_{22} \equiv k_2 R_2$, $\rho_{32} \equiv k_3 R_2$, so the coefficients determined by boundary conditions can be solved as follows:

$$D_1 = \frac{\begin{vmatrix} -\eta_l'(\rho_{11}) & \frac{\varepsilon_1}{\varepsilon_2} \zeta_l'(\rho_{21}) & \frac{\varepsilon_1}{\varepsilon_2} \eta_l'(\rho_{21}) & \zeta_l'(\rho_{11}) \\ -\frac{k_2}{k_1} \eta_l(\rho_{11}) & \zeta_l(\rho_{21}) & \eta_l(\rho_{21}) & \frac{k_2}{k_1} \zeta_l(\rho_{11}) \\ 0 & \frac{\varepsilon_3}{\varepsilon_2} \zeta_l'(\rho_{22}) & \frac{\varepsilon_3}{\varepsilon_2} \eta_l'(\rho_{22}) & 0 \\ 0 & \zeta_l(\rho_{22}) & \eta_l(\rho_{22}) & 0 \end{vmatrix}}{\begin{vmatrix} -\eta_l'(\rho_{11}) & \frac{\varepsilon_1}{\varepsilon_2} \zeta_l'(\rho_{21}) & \frac{\varepsilon_1}{\varepsilon_2} \eta_l'(\rho_{21}) & 0 \\ -\frac{k_2}{k_1} \eta_l(\rho_{11}) & \zeta_l(\rho_{21}) & \eta_l(\rho_{21}) & 0 \\ 0 & \frac{\varepsilon_3}{\varepsilon_2} \zeta_l'(\rho_{22}) & \frac{\varepsilon_3}{\varepsilon_2} \eta_l'(\rho_{22}) & -\xi_l'(\rho_{32}) \\ 0 & \zeta_l(\rho_{22}) & \eta_l(\rho_{22}) & -\frac{k_2}{k_3} \xi_l(\rho_{32}) \end{vmatrix}}. \quad (\text{B5})$$

Here, we only present the expression of D_1 . According to Cramer's rule, all the denominators of the coefficients are the same as the determinant of the coefficient matrix. If it were zero, the coefficients would take the maximum values resulting in the resonance of the cavity. Consequently, the general resonance conditions for the 2^l -TM modes of a bilayer spherical cavity embedded in an arbitrary medium are as follows:

$$\begin{vmatrix} -\eta_l'(\rho_{11}) & \frac{\varepsilon_1}{\varepsilon_2} \zeta_l'(\rho_{21}) & \frac{\varepsilon_1}{\varepsilon_2} \eta_l'(\rho_{21}) & 0 \\ -\frac{k_2}{k_1} \eta_l(\rho_{11}) & \zeta_l(\rho_{21}) & \eta_l(\rho_{21}) & 0 \\ 0 & \frac{\varepsilon_3}{\varepsilon_2} \zeta_l'(\rho_{22}) & \frac{\varepsilon_3}{\varepsilon_2} \eta_l'(\rho_{22}) & -\xi_l'(\rho_{32}) \\ 0 & \zeta_l(\rho_{22}) & \eta_l(\rho_{22}) & -\frac{k_2}{k_3} \xi_l(\rho_{32}) \end{vmatrix} = 0. \quad (\text{B6})$$

This equation can be simplified as

$$\frac{\begin{vmatrix} \frac{\varepsilon_3}{\varepsilon_2} \zeta'_l(\rho_{22}) & \xi'_l(\rho_{32}) \\ \zeta_l(\rho_{22}) & \frac{k_2}{k_3} \xi_l(\rho_{32}) \end{vmatrix}}{\begin{vmatrix} \frac{\varepsilon_3}{\varepsilon_2} \eta'_l(\rho_{22}) & \xi'_l(\rho_{32}) \\ \eta_l(\rho_{22}) & \frac{k_2}{k_3} \xi_l(\rho_{32}) \end{vmatrix}} = \frac{\begin{vmatrix} \frac{\varepsilon_1}{\varepsilon_2} \zeta'_l(\rho_{21}) & \eta'_l(\rho_{11}) \\ \zeta_l(\rho_{21}) & \frac{k_2}{k_1} \eta_l(\rho_{11}) \end{vmatrix}}{\begin{vmatrix} \frac{\varepsilon_1}{\varepsilon_2} \eta'_l(\rho_{21}) & \eta'_l(\rho_{11}) \\ \eta_l(\rho_{21}) & \frac{k_2}{k_1} \eta_l(\rho_{11}) \end{vmatrix}}. \quad (\text{B7})$$

For the 2^l -TE modes, based on the boundary conditions, we can get a set of linear equations:

$$\begin{aligned} B_2 \zeta'_l(\rho_{21}) + C_2 \eta'_l(\rho_{21}) &= \frac{\mu_2}{\mu_1} [\zeta'_l(\rho_{11}) + A_2 \eta'_l(\rho_{11})] \\ B_2 \zeta_l(\rho_{21}) + C_2 \eta_l(\rho_{21}) &= \frac{k_2}{k_1} [\zeta_l(\rho_{11}) + A_2 \eta_l(\rho_{11})] \\ B_2 \zeta'_l(\rho_{22}) + C_2 \eta'_l(\rho_{22}) &= \frac{\mu_2}{\mu_3} [D_2 \xi'_l(\rho_{32})] \\ B_2 \zeta_l(\rho_{22}) + C_2 \eta_l(\rho_{22}) &= \frac{k_2}{k_3} [D_2 \xi_l(\rho_{32})]. \end{aligned} \quad (\text{B8})$$

The resonance occurs when the determinant of the coefficient matrix is zero, which requires the following:

$$\begin{vmatrix} -\eta'_l(\rho_{11}) & \frac{\mu_1}{\mu_2} \zeta'_l(\rho_{21}) & \frac{\mu_1}{\mu_2} \eta'_l(\rho_{21}) & 0 \\ -\frac{k_2}{k_1} \eta_l(\rho_{11}) & \zeta_l(\rho_{21}) & \eta_l(\rho_{21}) & 0 \\ 0 & \frac{\mu_3}{\mu_2} \zeta'_l(\rho_{22}) & \frac{\mu_3}{\mu_2} \eta'_l(\rho_{22}) & -\xi'_l(\rho_{32}) \\ 0 & \zeta_l(\rho_{22}) & \eta_l(\rho_{22}) & -\frac{k_2}{k_3} \xi_l(\rho_{32}) \end{vmatrix} = 0. \quad (\text{B9})$$

This equation can be simplified as follows:

$$\frac{\begin{vmatrix} \frac{\mu_3}{\mu_2} \zeta'_l(\rho_{22}) & \xi'_l(\rho_{32}) \\ \zeta_l(\rho_{22}) & \frac{k_2}{k_3} \xi_l(\rho_{32}) \end{vmatrix}}{\begin{vmatrix} \frac{\mu_3}{\mu_2} \eta'_l(\rho_{22}) & \xi'_l(\rho_{32}) \\ \eta_l(\rho_{22}) & \frac{k_2}{k_3} \xi_l(\rho_{32}) \end{vmatrix}} = \frac{\begin{vmatrix} \frac{\mu_1}{\mu_2} \zeta'_l(\rho_{21}) & \eta'_l(\rho_{11}) \\ \zeta_l(\rho_{21}) & \frac{k_2}{k_1} \eta_l(\rho_{11}) \end{vmatrix}}{\begin{vmatrix} \frac{\mu_1}{\mu_2} \eta'_l(\rho_{21}) & \eta'_l(\rho_{11}) \\ \eta_l(\rho_{21}) & \frac{k_2}{k_1} \eta_l(\rho_{11}) \end{vmatrix}}, \quad (\text{B10})$$

which is the general solution when resonances occur for the TE modes.

APPENDIX C: PHASE DISTRIBUTION OF ELECTROMAGNETIC FIELDS IN THE ZIM

Take TM_{elm} mode as an example; the electromagnetic fields outside the cavities are

$$\begin{aligned} \mathbf{H}_{\text{TM}}^{ilm} &= D_1 \mathbf{M}_{ilm}^{(3)} = D_1 \left[-\sin(m\phi) \frac{m}{\sin\theta} P_{lm}(\cos\theta) \frac{\xi_l(k_3 r)}{k_3 r} \hat{\mathbf{e}}_\theta - \cos(m\phi) \frac{\partial P_{lm}(\cos\theta)}{\partial\theta} \frac{\xi_l(k_3 r)}{k_3 r} \hat{\mathbf{e}}_\phi \right], \\ \mathbf{E}_{\text{TM}}^{ilm} &= -\frac{k_3}{i\varepsilon_3 \varepsilon_0 \omega} D_1 \mathbf{N}_{ilm}^{(3)} = -\frac{k_3}{i\varepsilon_3 \varepsilon_0 \omega} D_1 \left[\frac{\xi_l(k_3 r)}{(k_3 r)^2} l(l+1) \cos(m\phi) P_{lm}(\cos\theta) \hat{\mathbf{e}}_r \right. \\ &\quad \left. + \frac{1}{kr} \xi'_l(k_3 r) \cos(m\phi) \frac{\partial P_{lm}(\cos\theta)}{\partial\theta} \hat{\mathbf{e}}_\theta + \frac{1}{kr} \xi'_l(k_3 r) (-\sin m\phi) \frac{m}{\sin\theta} P_{lm}(\cos\theta) \hat{\mathbf{e}}_\phi \right]. \end{aligned} \quad (\text{C1})$$

According to Eq. (3), substituting the expressions of $\xi_l(k_3 r)$ and $\xi'_l(k_3 r)$ into Eq. (C1), we can get

$$\begin{aligned} \mathbf{E}_\theta &= -\frac{k_3}{i\varepsilon_3 \varepsilon_0 \omega} D_1 \frac{1}{kr} \xi'_l(k_3 r) \cos(m\phi) \frac{\partial P_{lm}(\cos\theta)}{\partial\theta} = D_1 l \frac{\partial P_{lm}(\cos\theta)}{\partial\theta} \cos(m\phi) \frac{k_3}{\varepsilon_3 \varepsilon_0 \omega} a_0 (k_3 r)^{-l-2}, \\ \mathbf{H}_\phi &= -D_1 \cos(m\phi) \frac{\partial P_{lm}(\cos\theta)}{\partial\theta} \frac{\xi_l(k_3 r)}{k_3 r} = -D_1 \cos(m\phi) \frac{\partial P_{lm}(\cos\theta)}{\partial\theta} i a_0 (k_3 r)^{-l-1}. \end{aligned} \quad (\text{C2})$$

Here, we only show the θ component of the electric field and the ϕ component of the magnetic field. Interestingly, their phase will not change with r . In addition,

$$\frac{\mathbf{N}_{l\theta}^{(3)}}{\mathbf{M}_{l\phi}^{(3)}} = \frac{l}{k_3 r}, \quad \frac{\mathbf{E}_\theta}{\mathbf{H}_\phi} = i \frac{l}{\varepsilon_3 \varepsilon_0 \omega r}, \quad (\text{C3})$$

which means that the phase of the θ component of the electric field always lags behind the ϕ component of the magnetic field by $\pi/2$.

This peculiar property of phase leads to the ideal resonance of the cavity within the ZIM. The resonance condition of the bilayer cavities within an arbitrary medium can be

rewritten as

$$\frac{\begin{vmatrix} \frac{\varepsilon_3}{\varepsilon_2} \zeta'_l(\rho_{22}) & \frac{\xi'_l(\rho_{32})}{\xi_l(\rho_{32})} \\ \zeta_l(\rho_{22}) & \frac{k_2}{k_3} \end{vmatrix}}{\begin{vmatrix} \frac{\varepsilon_3}{\varepsilon_2} \eta'_l(\rho_{22}) & \frac{\xi'_l(\rho_{32})}{\xi_l(\rho_{32})} \\ \eta_l(\rho_{22}) & \frac{k_2}{k_3} \end{vmatrix}} = \frac{\begin{vmatrix} \frac{\varepsilon_1}{\varepsilon_2} \zeta'_l(\rho_{21}) & \eta'_l(\rho_{11}) \\ \zeta_l(\rho_{21}) & \frac{k_2}{k_1} \eta_l(\rho_{11}) \end{vmatrix}}{\begin{vmatrix} \frac{\varepsilon_1}{\varepsilon_2} \eta'_l(\rho_{21}) & \eta'_l(\rho_{11}) \\ \eta_l(\rho_{21}) & \frac{k_2}{k_1} \eta_l(\rho_{11}) \end{vmatrix}}. \quad (\text{C4})$$

According to Eq. (C4), this general case includes a term $\xi'_l(\rho_{32})/\xi_l(\rho_{32})$, which has imaginary components, so the frequency exactly satisfies that this equation is complex. However, based on Eq. (3), this term satisfies that $k_3 \xi'_l(\rho_{32})/\xi_l(\rho_{32}) = -l/R_2$ when the background is the ZIM. Therefore, the terms $\xi_l(\rho_{32})$ and $\xi'_l(\rho_{32})$ in the ZIM are in opposite phases so that the resonance condition does not have any imaginary component.

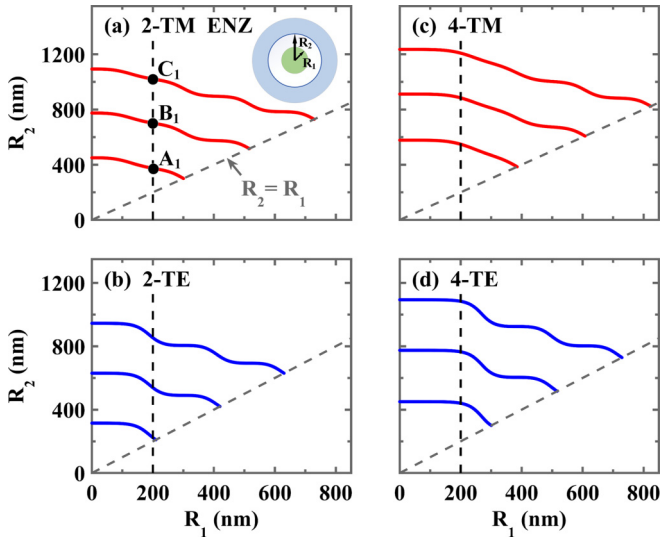


FIG. 7. The resonance conditions of the (a) 2-TM, (b) 2-TE, (c) 4-TM, and (d) 4-TE modes for the ENZ case. The curves have many branches, representing the multiplicity of solutions of the resonance condition, that is, resonance nesting. Here, $\lambda = 630$ nm, $\varepsilon_1 = 2.25$, $\mu_1 = 1$, $\varepsilon_2 = 1$, $\mu_2 = 1$, $\varepsilon_3 = 0$, $\mu_3 = 1$.

APPENDIX D: RESONANCE NESTING OF THE 2-TM, 2-TE, 4-TM, AND 4-TE MODES

1. For the ENZ background

According to Eqs. (5) and (7), the curves satisfying resonance conditions of the 2-TM, 2-TE, 4-TM, and 4-TE modes, respectively, can be obtained as shown in Fig. 7.

Figure 8 shows the electric field (modulus) distributions and normalized radiation power spectra at the nested points with $R_1 = 200$ nm. Based on these data and the analysis in the

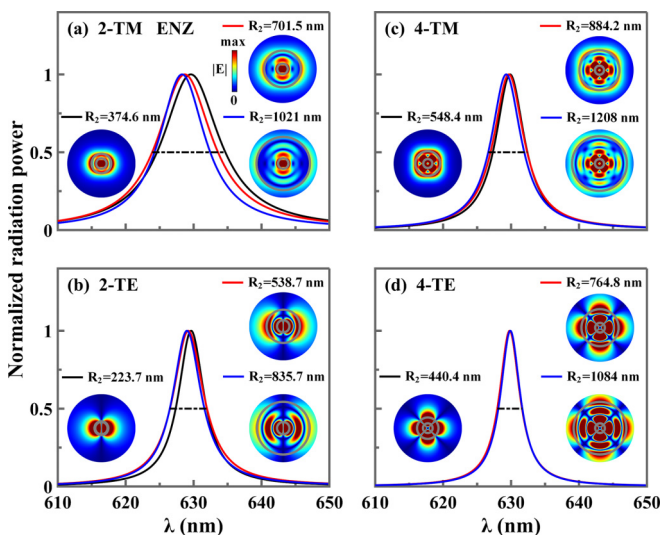


FIG. 8. Resonance nesting of the (a) 2-TM, (b) 2-TE, (c) 4-TM, and (d) 4-TE modes of a bilayer spherical cavity within an ENZ material. The insets are corresponding electric fields in cavities with different outer radius R_2 .

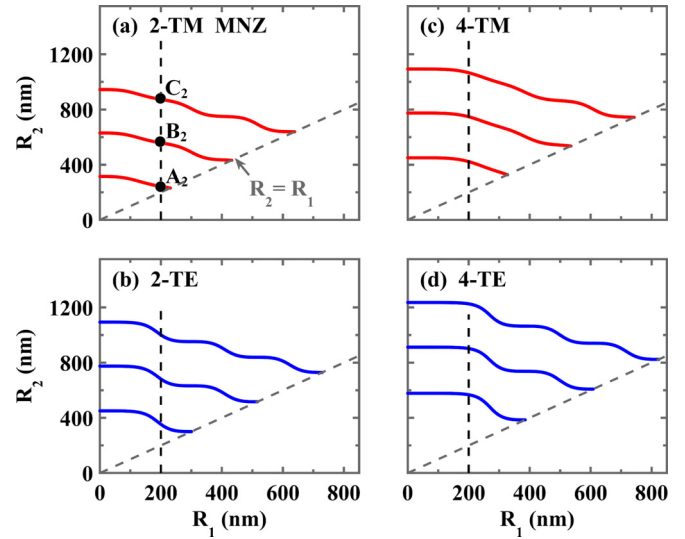


FIG. 9. The resonance conditions of the (a) 2-TM, (b) 2-TE, (c) 4-TM, and (d) 4-TE modes for the MNZ case. The curves have many branches, representing the multiplicity of solutions of the resonance condition, that is, resonance nesting. Here, $\varepsilon_3 = 1$, $\mu_3 = 0$, other parameters are the same as in Fig. 7.

main text, it is found that the resonance nesting effect widely exists in bilayer cavities within ENZ materials.

Moreover, the electric field distribution of the 2^l-TM mode is discontinuous at the interfaces due to the discontinuity of its radical component, which changes with the dielectric constant. Especially on the interface between cavity and ENZ, the electric field is drastically enhanced due to the ultrahigh contrast ratio of ε_2 and ε_3 , but for the 2^l-TE mode, the electric field is always continuous due to the boundary condition.

2. For the MNZ background

Then, the resonance nesting effect also appears in the monolayer cavities embedded in the MNZ background [32]. We expect that, given the same background, this effect should also be present in the bilayer cavities. According to Eqs. (4) and (8), the curves satisfying the resonance conditions of the 2-TM, 2-TE, 4-TM, and 4-TE modes, respectively, for the case where $\lambda = 630$ nm, $\varepsilon_1 = 2.25$, $\mu_1 = 1$, $\varepsilon_2 = 1$, $\mu_2 = 1$, $\varepsilon_3 = 1$, and $\mu_3 = 0$ can be obtained, as shown in Fig. 9. Taking the 2-TM mode as an example, the resonance curves have many branches, showing the existence of resonance nesting. The peaks of the radiation power spectra taken at nested points A_2 , B_2 , and C_2 with $R_1 = 200$ nm are nearly at 630 nm, as shown in Fig. 10(a). The insets of Fig. 10(a) show that the electric field distributions inside three cavities are perfectly consistent while just the number of wave nodes increases with R_2 . These provide further proof of resonance nesting's presence. Moreover, there are slight blueshifts of resonant wavelength in the radiation power spectra in Fig. 10(a) due to the imaginary part of $\mu_3 = 0.01i$. The results of the (b) 2-TE mode, (c) 4-TM mode, and (d) 4-TE mode are also shown in Figs. 9 and 10, which proves that the resonance nesting effect widely exists in bilayer cavity within MNZ materials.

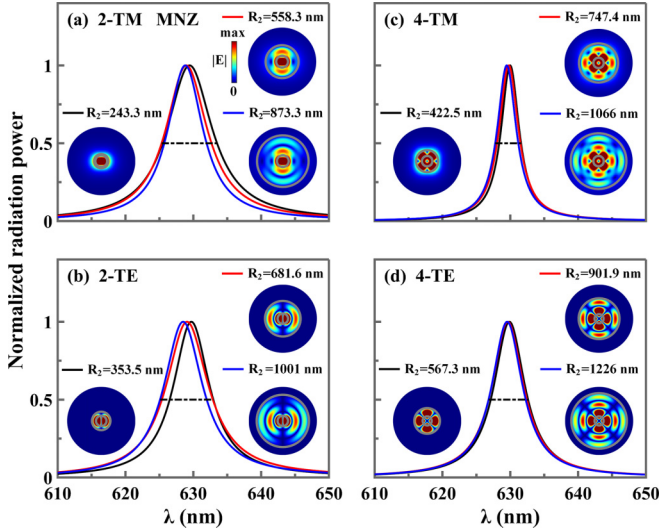


FIG. 10. The normalized power spectra and electric fields (modulus) of the (a) 2-TM, (b) 2-TE, (c) 4-TM, and (d) 4-TE modes at the nested points with $R_1 = 200$ nm. The peaks of resonance and the consistency of the electric field evidence the existence of resonance nesting.

Because the parameter is set as $\varepsilon_1 = 2.25$, $\varepsilon_2 = 1$, $\varepsilon_3 = 1$, the electric field discontinuity only happens at the interface between regions I and II for the TM modes. Especially, for the TE mode, the electric field outside the cavity is zero due to the extreme parameters of the MNZ material and the boundary condition at the interface between region II and the MNZ background.

3. For the EMNZ background

Next, inside the EMNZ background, monolayer cavities exhibit the resonance nesting effect too [32]. Considering the same background, we forecast that the same effect should exist in the bilayer cavities. According to Eqs. (5) and (8), the curves satisfying the resonance conditions of the 2-TM, 2-TE, 4-TM, and 4-TE modes, respectively, for the situation where $\lambda = 630$ nm, $\varepsilon_1 = 2.25$, $\mu_1 = 1$, $\varepsilon_2 = 1$, $\mu_2 = 1$, $\varepsilon_3 = 0$, and $\mu_3 = 0$ can be obtained, as shown in Fig. 11. Also, taking the 2-TM mode as an example, the resonance curves have many branches, showing the existence of resonance nesting. The peaks of the radiation power spectra taken at nested points A_2 , B_2 , and C_2 with $R_1 = 200$ nm are approximately at 630 nm, as shown in Fig. 12(a). The insets of Fig. 12(a) show that only the number of wave nodes increases with R_2 , with no further changes in the electric field distributions inside three cavities. These provide proof that resonance nesting occurs. Moreover, different from the ENZ case, the resonant wavelength shifts from 630 nm are very small because the $\varepsilon_3 = 0.01i$, $\mu_3 = 0.01i$, and $n_3 = \sqrt{\varepsilon_3\mu_3}$ are all near zero.

The results of the (b) 2-TE mode, (c) 4-TM mode, and (d) 4-TE mode are also shown in Figs. 11 and 12, which prove that the resonance nesting effect widely exists in a bilayer cavity within EMNZ materials. Moreover, as already inferred by Eqs. (5) and (8), the curves of the 2^l -TM modes for the EMNZ case are the same as those for the ENZ case, and the curves of the 2^l -TE modes for the EMNZ case are the same

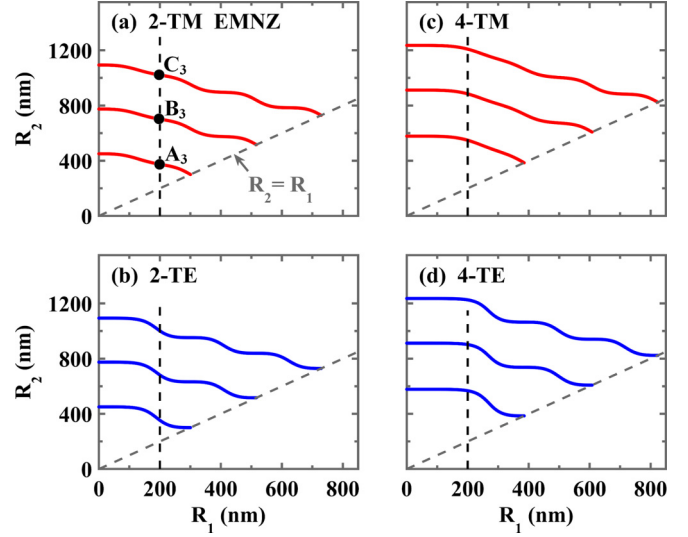


FIG. 11. The resonance conditions of the (a) 2-TM, (b) 2-TE, (c) 4-TM, and (d) 4-TE modes for the EMNZ case. The curves have many branches, representing the multiplicity of solutions of the resonance condition, that is, resonance nesting. Here, $\varepsilon_3 = 0$, $\mu_3 = 0$; other parameters are the same as in Fig. 7.

as those for the MNZ case. By comparing the electric field distributions for the EMNZ, ENZ, and MNZ cases, we can find that the electric field of the TM mode for the EMNZ case is the same as that for the ENZ case, and the electric field of the TE mode for the EMNZ case is the same as that for the MNZ case.

APPENDIX E: MODE DEGENERACY

1. Mode degeneracy at nested points for the ENZ background

For the ENZ background, the degeneracy between the 2-TM and 4-TE modes exists at the nested points, such as A_4 ,

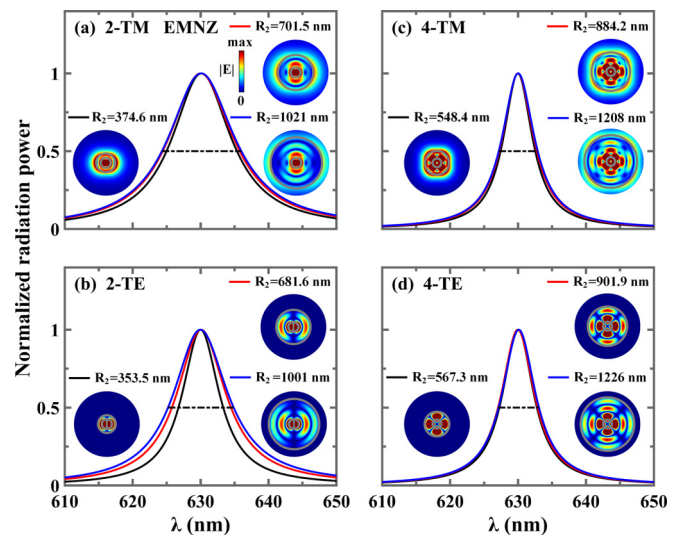


FIG. 12. The normalized power spectra and electric fields (modulus) of the (a) 2-TM, (b) 2-TE, (c) 4-TM, and (d) 4-TE modes at the nested points with $R_1 = 200$ nm. The peaks of resonance and the consistency of the electric field evidence the existence of resonance nesting.

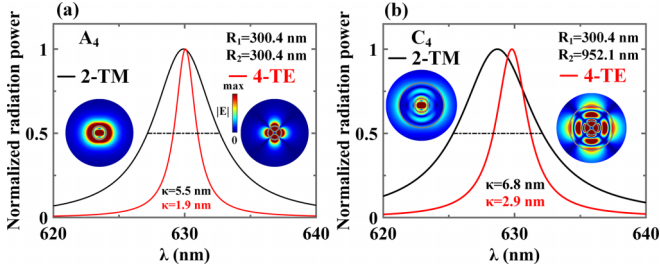


FIG. 13. The normalized radiation power spectra of the 2-TM and 4-TE modes at points A_4 and C_4 . The insets are corresponding electric field distributions (modulus).

B_4 , and C_4 in Fig. 4(a). Figure 13 shows the electric field distributions and normalized radiation power spectra at the nested degenerate points A_4 and C_4 . These results demonstrate the nested nature of degenerate points.

2. Mode degeneracy effect of a bilayer spherical cavity within the MNZ background

The mode degeneracy between the 2^{l+1} -TM and 2^l -TE modes exists in monolayer spherical cavities within the MNZ background [32]. With the same background, it seems that the bilayer cavities should also exhibit such effect, but from the following analysis, we found that the situation is very different; i.e., the 2^{l+1} -TM and 2^l -TE modes of bilayer cavities within the MNZ material are degenerated only at some special nested points. In what follows, we first analytically prove this based on the resonance conditions. According to Eqs. (4) and (12), the 2^{l+1} -TM modes satisfy the following:

$$\frac{\zeta_l(\rho_{22})}{\eta_l(\rho_{22})} = \frac{\begin{vmatrix} \frac{\varepsilon_1}{\varepsilon_2} \zeta'_{l+1}(\rho_{21}) & \eta'_{l+1}(\rho_{11}) \\ \zeta_{l+1}(\rho_{21}) & \frac{k_2}{k_1} \eta_{l+1}(\rho_{11}) \end{vmatrix}}{\begin{vmatrix} \frac{\varepsilon_1}{\varepsilon_2} \eta'_{l+1}(\rho_{21}) & \eta'_{l+1}(\rho_{11}) \\ \eta_{l+1}(\rho_{21}) & \frac{k_2}{k_1} \eta_{l+1}(\rho_{11}) \end{vmatrix}}. \quad (\text{E1})$$

By comparing Eq. (E1) with Eq. (8), it is found that the left-hand sides (LHSs) of the resonance conditions of the 2^{l+1} -TM and 2^l -TE modes are the same but the right-hand sides (RHSs) are often unequal. For some unique R_1 , they can be the same, allowing these two modes to be degenerate. Similar to the ENZ situation, if a resonant cavity satisfies the degeneracy criterion, all of the resonant cavities nested with it do as well.

Next, take the 4-TM and 2-TE modes as an example. As shown by the resonance condition curves in Fig. 14(a), the degeneracy exists in bilayer cavities at some nested degenerate points such as A_5 and B_5 with $R_1 = 385.3$ nm. A difference between the MNZ and ENZ cases is that the 4-TM and 2-TE modes are not degenerated in those cavities with $R_1 = R_2 \neq 0$, because $\varepsilon_3 \neq \varepsilon_1$. The normalized radiation power spectra at the degenerate point A_5 are shown in Fig. 14(b). The peaks of the power spectra are almost at 630 nm, representing the establishment of mode degeneracy. Additionally, the 4-TM mode's linewidth and slight blueshift from the ideal resonant wavelength (630 nm) are smaller than the counterpart of the 2-TE mode because the higher-order mode suffers from less radiation loss. Moreover, as Fig. 15 shows, the cavities at the

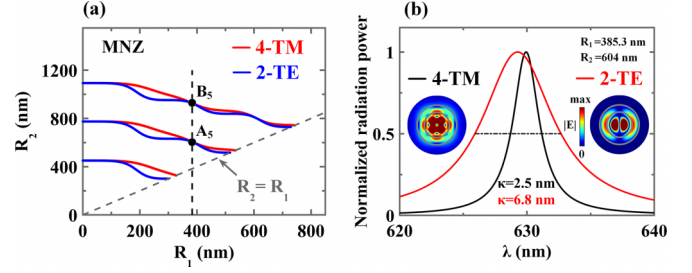


FIG. 14. The degeneracy between the 4-TM and 2-TE modes of bilayer spherical cavities for the MNZ case. (a) The resonance conditions of the 4-TM and 2-TE modes. The nested points where the red curves intersect with the blue curves represent the degeneracy. (b) The normalized radiation power spectra of the 4-TM and 2-TE modes at point A_5 . The insets are corresponding electric field distributions (modulus).

nested point B_5 also exhibit the same results, demonstrating the nesting nature of degenerate points. Therefore, for the MNZ case, the 2^{l+1} -TM and 2^l -TE modes of bilayer cavities at some special nested points will be degenerated.

3. Mode degeneracy effect of a bilayer spherical cavity within the EMNZ background

In the monolayer spherical cavities within EMNZ background, there is mode degeneracy between the 2^l -TM and 2^l -TE modes [32]. This effect would seem to be expected in a bilayer cavity given the same background. The following results reveal that the situation is different; that is, the 2^l -TM and 2^l -TE modes of bilayer cavities within the EMNZ material are only degenerated at some nested points. In what follows, we first analytically prove this conclusion based on the resonance conditions. By comparing Eq. (5) with Eq. (8), it is found that the left-hand sides (LHSs) of the resonance conditions of the 2^l -TM and 2^l -TE modes are the same but the right-hand sides (RHSs) are usually not equal. For some special R_1 , they can be the same, allowing these two modes to be degenerate. Similar to the ENZ and MNZ cases, if a resonant cavity satisfies the degeneracy criterion, so do all of the nested resonant cavities. Then, take the 2-TM and 2-TE modes as an example. The

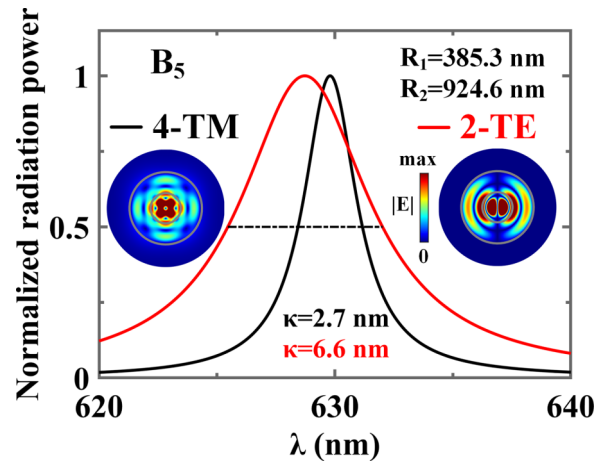


FIG. 15. The normalized radiation power spectra at point B_5 . The insets are corresponding electric field distributions (modulus).

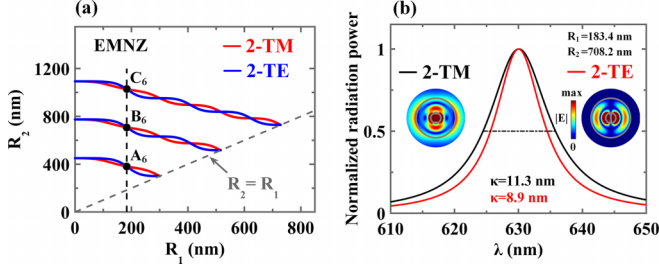


FIG. 16. The degeneracy between the 2-TM and 2-TE modes of bilayer spherical cavities for the EMNZ case. (a) The resonance conditions of the 2-TM and 2-TE modes. The nested points where the red curves intersect with the blue curves represent the degeneracy. (b) The normalized radiation power spectra of the 2-TM and 2-TE modes at point B_6 . The insets are corresponding electric field distributions (modulus).

resonance condition curves are plotted in Fig. 16(a). It is found that the degeneracy exists in bilayer spherical cavities at some nested degenerate points such as A_6 , B_6 , and C_6 with $R_1 = 183.4$ nm. The normalized radiation power spectra at point B_6 are shown in Fig. 16(b). The peaks of the power spectra are almost at 630 nm, representing the establishment of mode degeneracy. Additionally, the resonant wavelength is very close to the ideal wavelength (630 nm) because the imaginary parts of ϵ_3 and μ_3 are both very small. Moreover, as Fig. 17 shows, the cavities at the nested points A_6 and C_6 also exhibit the same results, demonstrating the nesting nature of degenerate points. So, for the EMNZ case, the 2^l -TM and 2^l -TE modes of bilayer cavities at some special nested points will be degenerated.

APPENDIX F: ELECTRIC FIELD DISTRIBUTION ON RESONANCE OF TE MODES

For TE modes, the new expression of the electromagnetic field is

$$\mathbf{E}_{\text{TE}}^{ilm} = \begin{cases} \mathbf{M}_{ilm}^{(1)}, & r < R_1 \\ b_2 \mathbf{M}_{ilm}^{(2)} + c_2 \mathbf{M}_{ilm}^{(1)}, & R_1 < r < R_2, \\ d_2 \mathbf{M}_{ilm}^{(3)}, & r > R_2 \end{cases} \quad (\text{F1})$$

$$\mathbf{H}_{\text{TE}}^{ilm} = \begin{cases} \frac{k_1}{i\mu_1 \epsilon_0 \omega} \mathbf{N}_{ilm}^{(1)}, & r < R_1 \\ \frac{k_2}{i\mu_2 \epsilon_0 \omega} (b_2 \mathbf{N}_{ilm}^{(2)} + c_2 \mathbf{N}_{ilm}^{(1)}), & R_1 < r < R_2, \\ \frac{k_3}{i\mu_3 \epsilon_0 \omega} d_2 \mathbf{N}_{ilm}^{(3)}, & r > R_2 \end{cases}$$

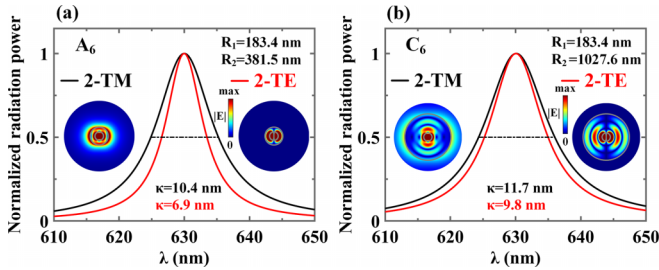


FIG. 17. The normalized radiation power spectra at points A_6 and C_6 . The insets are corresponding electric field distributions (modulus).

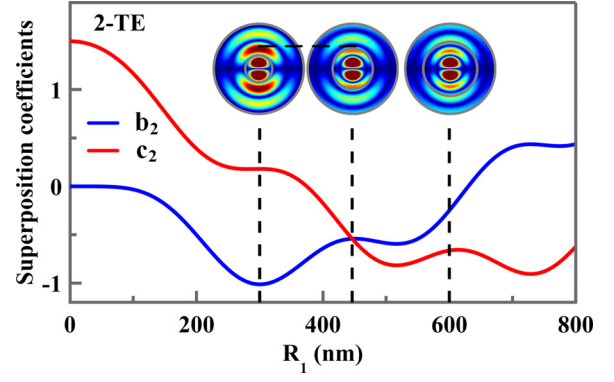


FIG. 18. The superposition coefficients of the field in region II for the 2-TE mode. The variation of superposition coefficients results in the modulation of the electric field distribution. The insets are corresponding electric fields at different R_1 .

where b_2 , c_2 are the new coefficients. By substituting the resonance conditions into it, we can get

$$b_2 = \frac{\begin{vmatrix} \eta'_l(\rho_{11}) & \frac{\mu_1}{\mu_2} \eta'_l(\rho_{21}) \\ \frac{k_2}{k_1} \eta_l(\rho_{11}) & \eta_l(\rho_{21}) \end{vmatrix}}{\begin{vmatrix} \frac{\mu_1}{\mu_2} \zeta'_l(\rho_{21}) & \frac{\mu_1}{\mu_2} \eta'_l(\rho_{21}) \\ \zeta_l(\rho_{21}) & \eta_l(\rho_{21}) \end{vmatrix}};$$

$$c_2 = \frac{\begin{vmatrix} \eta'_l(\rho_{11}) & \frac{\mu_1}{\mu_2} \zeta'_l(\rho_{21}) \\ \frac{k_2}{k_1} \eta_l(\rho_{11}) & \zeta_l(\rho_{21}) \end{vmatrix}}{\begin{vmatrix} -\frac{\mu_1}{\mu_2} \zeta'_l(\rho_{21}) & -\frac{\mu_1}{\mu_2} \eta'_l(\rho_{21}) \\ \zeta_l(\rho_{21}) & \eta_l(\rho_{21}) \end{vmatrix}}. \quad (\text{F2})$$

The relationship between coefficients and R_1 and the corresponding electric field distributions for the 2-TE mode are shown in Fig. 18.

APPENDIX G: VERIFICATION OF ANALYTICAL RESULTS BY NUMERICAL SIMULATIONS

To validate the aforementioned analytic results, we do a three-dimensional finite element simulation using commercial COMSOL MULTIPHYSICS software. We construct the system's geometrical structure first, as seen in Fig. 19. For the purpose of reducing the scattering field and simulating endless space,

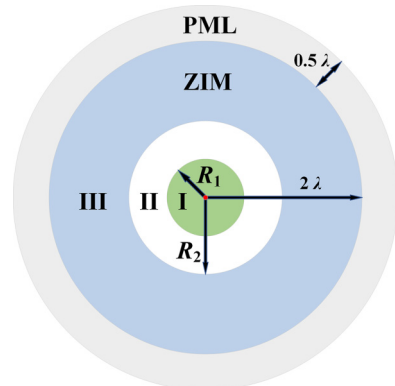


FIG. 19. The sketch map of the simulation module by COMSOL.

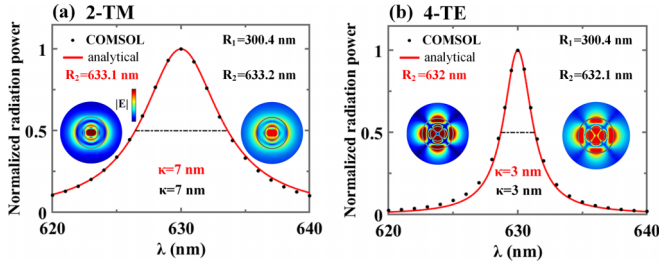


FIG. 20. The normalized radiation power spectra and electric field distributions obtained using the analytical method and numerical method, respectively, for the ENZ case. Here, $\epsilon_3 = 0.01i$, $\mu_3 = 1$.

the infinite ZIM is configured as a sphere with $R = 2\lambda$ and is encircled by a perfect match layer (PML) with a thickness of 0.5λ . Here, λ is 630 nm which is set as the ZIM wavelength. The combination of the light green part and the white part in Fig. 19 is a bilayer spherical dielectric cavity. Region I is a sphere with the radius R_1 , dielectric constant ϵ_1 , and permeability μ_1 , and region II is a spherical shell with the thickness $R_2 - R_1$, dielectric constant ϵ_2 , and permeability μ_2 . Then, an electric dipole with z polarization is put in the cavity to excite the eigenmode. In this module, the dipole is modeling as a point with a specific dipole moment. For all finite element methods, the structure needs to be divided into meshes. Here, region II of the bilayer spherical cavity and the ZIM background are separated into some free tetrahedra with maximum sizes of $\lambda/6$ and minimum sizes of 0.4 nm, whereas region I is divided in accordance with the particular inner radius. In order to simply compute the radiation power, a tiny sphere (the radius is 5 nm) is placed outside the dipole. We have confirmed that this module is accurate, as done in our previous work [32]. In what follows, we will compare the power spectra and electric field distributions obtained using the analytical method with those obtained using the simulation method in order to validate the analytical results. The electromagnetic parameters of regions I and II are $\epsilon_1 = 2.25$, $\mu_1 = 1$, and $\epsilon_2 = 1$, $\mu_2 = 1$, respectively.

1. Simulation verification for the ENZ background

We verify the results at a degenerate point of the 2-TM and 4-TE modes for the ENZ case. The configuration of a selected degenerate point is $R_1 = 300.4$ nm, $R_2 = 631.8$ nm by ignoring the loss of the ENZ background. The normalized radiation power spectra and electric field distributions obtained using the analytical method and numerical method are shown in Fig. 20.

The parameters of the ENZ background are $\epsilon_3 = 0.01i$, $\mu_3 = 1$ here. The resonant wavelength of the radiation power spectrum drawn using the ideal radius configuration ($R_1 = 300.4$ nm, $R_2 = 631.8$ nm) will deviate slightly from the ideal resonant wavelength (630 nm). Therefore, in order to make the comparison more intuitive, the analysis result adopted the configuration which is slightly different from the ideal value. Altogether, the simulation results are in very good agreement with the analytical results.

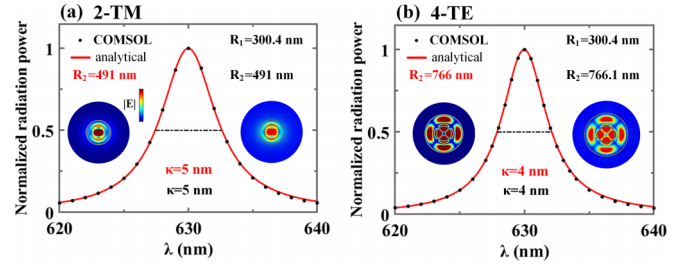


FIG. 21. The normalized radiation power spectra and electric field distributions obtained using the analytical method and numerical method, respectively, for the MNZ case. Here, $\mu_3 = 0.01i$, $\epsilon_3 = 1$.

2. Simulation verification for the MNZ background

We verify the results at a specific resonance configuration with $R_1 = 300.4$ nm, $R_2 = 490.1$ nm for the 2-TM mode and at a configuration with $R_1 = 300.4$ nm, $R_2 = 765.8$ nm for the 4-TE mode when ignoring the loss of the MNZ background. The normalized radiation power spectra and electric field distributions obtained using the analytical method and numerical method are shown in Fig. 21. Altogether, the simulation results are in very good agreement with the analytical results.

3. Simulation verification for the EMNZ background

We verify the results at a specific resonance configuration with $R_1 = 250$ nm, $R_2 = 351$ nm for the 2-TM mode when ignoring the loss of the EMNZ background. The normalized radiation power spectra and electric field distributions obtained using the analytical method and numerical method are shown in Fig. 22. Altogether, the simulation results are in very good agreement with the analytical results.

In a word, regardless of the background, the analysis results are well matched with the simulation results, which greatly improves the reliability of the analysis results.

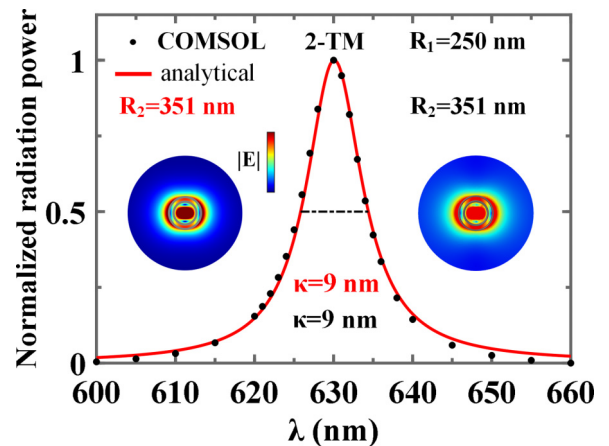


FIG. 22. The normalized radiation power spectra and electric field distributions obtained using the analytical method and numerical method, respectively, for the EMNZ case. Here, $\mu_3 = 0.01i$, $\epsilon_3 = 0.01i$.

- [1] G. V. Naik, V. M. Shalaev, and A. Boltasseva, Alternative plasmonic materials: Beyond gold and silver, *Adv. Mater.* **25**, 3264 (2013).
- [2] Y. Wang, A. Capretti, and L. D. Negro, Wide tuning of the optical and structural properties of alternative plasmonic materials, *Opt. Mater. Express* **5**, 2415 (2015).
- [3] N. Kinsey, C. DeVault, J. Kim, M. Ferrera, V. M. Shalaev, and A. Boltasseva, Epsilon-near-zero Al-doped ZnO for ultrafast switching at telecom wavelengths, *Optica* **2**, 616 (2015).
- [4] M. Z. Alam, I. De Leon, and R. W. Boyd, Large optical nonlinearity of indium tin oxide in its epsilon-near-zero region, *Science* **352**, 795 (2016).
- [5] J. D. Caldwell, O. J. Glembocki, Y. Francescato, N. Sharac, V. Giannini, F. J. Bezares, J. P. Long, J. C. Owrutsky, I. Vurgaftman, J. G. Tischler *et al.*, Low-loss, extreme subdiffraction photon confinement via silicon carbide localized surface phonon polariton resonators, *Nano Lett.* **13**, 3690 (2013).
- [6] W. Streyer, K. Feng, Y. Zhong, A. J. Hoffman, and D. Wasserman, Engineering the reststrahlen band with hybrid plasmon/phonon excitations, *MRS Commun.* **6**, 1 (2016).
- [7] E. J. R. Vesseur, T. Coenen, H. Caglayan, N. Engheta, and A. Polman, Experimental Verification of $n = 0$ Structures for Visible Light, *Phys. Rev. Lett.* **110**, 013902 (2013).
- [8] N. Garcia, E. V. Ponizovskaya, and J. Q. Xiao, Zero permittivity materials: Band gaps at the visible, *Appl. Phys. Lett.* **80**, 1120 (2002).
- [9] X. Huang, Y. Lai, Z. H. Hang, H. Zheng, and C. T. Chan, Dirac cones induced by accidental degeneracy in photonic crystals and zero-refractive-index materials, *Nat. Mater.* **10**, 582 (2011).
- [10] G. Subramania, A. J. Fischer, and T. S. Luk, Optical properties of metal-dielectric based epsilon near zero metamaterials, *Appl. Phys. Lett.* **101**, 241107 (2012).
- [11] R. Maas, J. Parsons, N. Engheta, and A. Polman, Experimental realization of an epsilon-near-zero metamaterial at visible wavelengths, *Nat. Photonics* **7**, 907 (2013).
- [12] S. Enoch, G. Tayeb, P. Sabouroux, N. Guérin, and P. Vincent, A Metamaterial for Directive Emission, *Phys. Rev. Lett.* **89**, 213902 (2002).
- [13] R. W. Ziolkowski, Propagation in and scattering from a matched metamaterial having a zero index of refraction, *Phys. Rev. E* **70**, 046608 (2004).
- [14] Y. Yuan, L. Shen, L. Ran, T. Jiang, J. Huangfu, and J. A. Kong, Directive emission based on anisotropic metamaterials, *Phys. Rev. A* **77**, 053821 (2008).
- [15] M. G. Silveirinha and N. Engheta, Theory of supercoupling, squeezing wave energy, and field confinement in narrow channels and tight bends using ϵ near-zero metamaterials, *Phys. Rev. B* **76**, 245109 (2007).
- [16] M. Silveirinha and N. Engheta, Tunneling of Electromagnetic Energy through Subwavelength Channels and Bends Using ϵ -Near-Zero Materials, *Phys. Rev. Lett.* **97**, 157403 (2006).
- [17] J. S. Marcos, M. G. Silveirinha, and N. Engheta, μ -near-zero supercoupling, *Phys. Rev. B* **91**, 195112 (2015).
- [18] M. Z. Alam, S. A. Schulz, J. Upham, I. De Leon, and R. W. Boyd, Large optical nonlinearity of nanoantennas coupled to an epsilon-near-zero material, *Nat. Photonics* **12**, 79 (2018).
- [19] A. R. Davoyan, A. M. Mahmoud, and N. Engheta, Optical isolation with epsilon-near-zero metamaterials, *Opt. Express* **21**, 3279 (2013).
- [20] A. R. Davoyan and N. Engheta, Theory of Wave Propagation in Magnetized Near-Zero-Epsilon Metamaterials: Evidence for One-Way Photonic States and Magnetically Switched Transparency and Opacity, *Phys. Rev. Lett.* **111**, 257401 (2013).
- [21] H. N. S. Krishnamoorthy, Z. Jacob, E. Narimanov, I. Kretzschmar, and V. M. Menon, Topological transitions in metamaterials, *Science* **336**, 205 (2012).
- [22] J. Kim, A. Dutta, G. V. Naik, A. J. Giles, F. J. Bezares, C. T. Ellis, J. G. Tischler, A. M. Mahmoud, H. Caglayan, O. J. Glembocki *et al.*, Role of epsilon-near-zero substrates in the optical response of plasmonic antennas, *Optica* **3**, 339 (2016).
- [23] S. A. Schulz, A. A. Tahir, M. Z. Alam, J. Upham, I. De Leon, and R. W. Boyd, Optical response of dipole antennas on an epsilon-near-zero substrate, *Phys. Rev. A* **93**, 063846 (2016).
- [24] A. Alù, M. G. Silveirinha, A. Salandrino, and N. Engheta, Epsilon-near-zero metamaterials and electromagnetic sources: Tailoring the radiation phase pattern, *Phys. Rev. B* **75**, 155410 (2007).
- [25] H. Chu, Q. Li, B. Liu, J. Luo, S. Sun, Z. H. Hang, L. Zhou, and Y. Lai, A hybrid invisibility cloak based on integration of transparent metasurfaces and zero-index materials, *Light Sci. Appl.* **7**, 50 (2018).
- [26] N. Engheta, Circuits with light at nanoscales: Optical nanocircuits inspired by metamaterials, *Science* **317**, 1698 (2007).
- [27] Y. Li, I. Liberal, C. Della Giovampaola, and N. Engheta, Waveguide metatronics: Lumped circuitry based on structural dispersion, *Sci. Adv.* **2**, e1501790 (2016).
- [28] J. Luo, P. Xu, H. Chen, B. Hou, L. Gao, and Y. Lai, Realizing almost perfect bending waveguides with anisotropic epsilon-near-zero metamaterials, *Appl. Phys. Lett.* **100**, 221903 (2012).
- [29] H. F. Ma, J. H. Shi, W. X. Jiang, and T. J. Cui, Experimental realization of bending waveguide using anisotropic zero-index materials, *Appl. Phys. Lett.* **101**, 253513 (2012).
- [30] I. Liberal, A. M. Mahmoud, and N. Engheta, Geometry-invariant resonant cavities, *Nat. Commun.* **7**, 10989 (2016).
- [31] I. Liberal and N. Engheta, Nonradiating and radiating modes excited by quantum emitters in open epsilon-near-zero cavities, *Sci. Adv.* **2**, e1600987 (2016).
- [32] X. Duan, H. Chen, Y. Ma, Z. Qian, Q. Zhang, Y. Lai, R. Peng, Q. Gong, and Y. Gu, Nesting and degeneracy of Mie resonances of dielectric cavities within zero-index materials, *J. Opt.* **24**, 025401 (2022).
- [33] E. Prodan, C. Radloff, N. J. Halas, and P. Nordlander, A hybridization model for the plasmon response of complex nanostructures, *Science* **302**, 419 (2003).
- [34] C. Radloff and N. J. Halas, Plasmonic properties of concentric nanoshells, *Nano Lett.* **4**, 1323 (2004).
- [35] G. Mie, Beiträge zur optik trüber medien, speziell kolloidaler metallösungen, *Ann. Phys.* **330**, 377 (1908).
- [36] P. Debye, Zur theorie der spezifischen wärmen, *Ann. Phys.* **344**, 789 (1912).
- [37] Y. Ma, Q. Liu, L. Shan, X. Zhang, Y. Jia, Q. Gong, and Y. Gu, Inhibition and enhancement of the spontaneous emission in spherical cavities surrounded by zero-index-materials, *Phys. Chem. Chem. Phys.* **25**, 16835 (2023).
- [38] Y. Li and C. Argyropoulos, Multiqubit entanglement and quantum phase gates with epsilon-near-zero plasmonic waveguides, *Appl. Phys. Lett.* **119**, 211104 (2021).